ADVANCED MATERIALS
www.advmat.de

Multileveled Hierarchical Hydrogel with Continuous Biophysical and Biochemical Gradients for Enhanced Repair of Full-Thickness Osteochondral Defect

Liwen Zhang, Wenli Dai, Chenyuan Gao, Wei Wei, Ruiran Huang, Xin Zhang, Yingjie Yu,* Xiaoping Yang, and Qing Cai**

The repair of hierarchical osteochondral defect requires sophisticated gradient reestablishment; however, few strategies for continuous gradient casting consider the relevance to clinical practice regarding cell adaptability, multiple gradient elements, and precise gradient mirroring native tissue. Here, a hydrogel with continuous gradients in nano-hydroxyapatite (HA) content, mechanical, and magnetism is developed using synthesized superparamagnetic HA nanorods (MagHA) that easily respond to a brief magnetic field. To precisely reconstruct osteochondral tissue, the optimized gradient mode is calculated according to magnetic resonance imaging (MRI) of healthy rabbit knees. Then, MagHA are patterned to form continuous biophysical and biochemical gradients, consequently generating incremental HA, mechanical, and electromagnetic cues under an external magnetic stimulus. To make such depth-dependent biocues work, an adaptable hydrogel is developed to facilitate cell infiltration. Furthermore, this approach is applied in rabbit full-thickness osteochondral defects equipped with a local magnetic field. Surprisingly, this multileveled gradient composite hydrogel repairs osteochondral unit in a perfect heterogeneous feature, which mimics the gradual cartilage-to-subchondral transition. Collectively, this is the first study that combines an adaptable hydrogel with magneto-driven MagHA gradients to achieve promising outcomes in osteochondral regeneration.

1. Introduction

Full-thickness defect in osteochondral tissue, a typical interfacial tissue in joints, is hard to be restored after trauma-related injuries or osteoarthritis (OA).[1,2] The challenge of osteochondral repair stems from the reconstruction of various multileveled and continuous gradients in connective tissue, which mainly include the gradients in biochemical compositions (e.g., collagen, inorganic component, and cell types) and biophysical conditions (e.g., stiffness and electromagnetic biophysics).[3,4]

Hydroxyapatite (HA), a calcium phosphate mineral, constructs the main compositional and mechanical gradients in osteochondral tissue. Notably, both gradients vary in a gradual rather than a sharp mode, thus forming a stable interface to connect the cartilage and subchondral bone in the maturated joint. The interface provides a smooth functional transition between the two distinguished parts. Hence, such an unique physiological feature of osteochondral tissueproposes two basic requirements for the design of implanted scaffold: 1) Adequate cell supply to reconstruct tissue; 2) Biochemical and biophysical microenvironment precisely matching with native tissue and guiding cell fates.[5,6–8] The bone marrow cavity beneath the full-thickness osteochondral injury can provide the cell source to support tissue regeneration, while requiring a scaffold to allow cell infiltration.[9]

L. Zhang, C. Gao, W. Wei, R. Huang, Y. Yu, X. Yang, Q. Cai
State Key Laboratory of Organic-Inorganic Composites
Beijing Laboratory of Biomedical Materials
Beijing University of Chemical Technology
Beijing 100029, China
E-mail: yuyingjie@mail.buct.edu.cn; caiqing@mail.buct.edu.cn
L. Zhang
MOE Key Laboratory of Macromolecular Synthesis and Functionalization Department of Polymer Science and Engineering
Zhejiang University
Hangzhou 310027, China
W. Dai
Peking University Third Hospital
Beijing 100191, China
X. Zhang
Institute of Sports Medicine
Beijing Key Laboratory of Sports Injuries
Peking University Third Hospital
Beijing 100191, China
E-mail: Xinzhang0805@Bimini.edu.cn
The ORCID identification number(s) for the author(s) of this article can be found under https://doi.org/10.1002/adma.202209565.

DOI: 10.1002/adma.202209565

Hydrogel matrix with a similar structure to that of extracellular matrix (ECM) is an ideal carrier of hierarchical signals and patterns owing to its controllable and triggerable sol-gel transition.[5,10,11] However, most covalently-crosslinked hydrogel network hinder cell migrations. Reversible crosslinking network is highlighted since it can be reformed by cell traction to favor cell movement associated with its fast stress relaxation.[12–17] The binding force between cyclodextrin and aromatic ring has been evidenced weak to be remodeled by cell skeleton. Here, an adaptable double-network (DN) hydrogel crosslinked via partial covalent bonds and partial host-guest interactions provided a suitable niche to recruit stem cells from bone marrow cavity.[18,19]

Importantly, a scaffold should provide tissue-specific signals to guide cell differentiation.[8] Although various bi-phasic and multi-layered scaffolds have been developed to construct the cartilage-to-subchondral gradient, it is still challenging to combine both continuous biochemical and biophysical cues in the same scaffold for osteochondral tissue regeneration.[5,10] Of note, these discontinuous and abrupt interfaces between layers may lead to delamination, making it difficult to restore the heterogeneous nature of osteochondral tissues.[11,20] Scaffolds with continuous biomimetic gradients have emerged as an ideal solution to tackle the challenges.[5,10,21,22] To accomplish the nano-scaled fabrication, grafts with integrally-formed continuous gradient have been prepared using buoyancy, electric, acoustic, light, and magnetic techniques.[23–28] Whereas the relevance between those gradient structures and realistic demands remains unknown.

Herein, we applied the magnetic field to pattern superparamagnetic HA nanorods (MagHA) within adaptable DN hydrogel to integrally form multileveled (compositional, mechanical, and magnetism) gradients targeting osteochondral regeneration (**Scheme 1**). The DN hydrogel consisted of gelatin methacryloyl (GelMA) and acrylate β-cyclodextrin (AcCD). Superparamagnetic Fe_3O_4 nanoparticles (NPs) were embedded in HA nanorods via the chemical precipitation method to form MagHA.[29,30] Under a magnetic field, these nano-scaled MagHA moved downward in the pre-hydrogel solution vertically to generate an incremental content gradation which was fixed after hydrogel crosslinking, as the MagHA being modified with reactive acrylate group and forming covalent bonds with polymeric chains. This MagHA distribution resembles the continuous low-to-high mineral, mechanical and electromagnetic biophysics gradient existing in native osteochondral tissue from the superficial zone (top) to the subchondral bone zone (bottom), hence providing an adaptable composite hydrogel system to facilitate cell infiltration and site-specific differentiation. To the best of our knowledge, the concept of using such a continuous MagHA gradient has never been tested in repair of osteochondral defects.

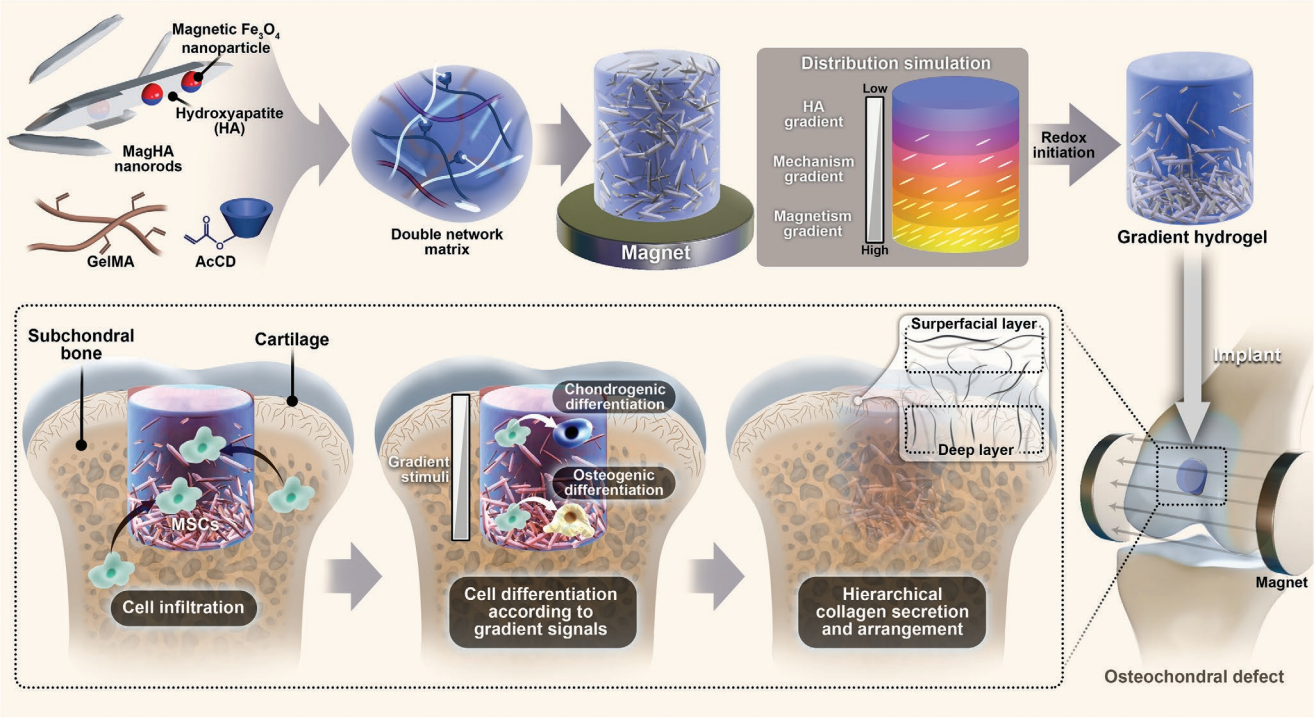

Scheme 1. The design and application of multileveled continuous gradient hydrogel for the repair of osteochondral defect. A) schematic illustration shows that a gradient hydrogel consists of inorganic superparamagnetic HA nanorods (MagHA) having superparamagnetic nanocores and organic gelatin methacryloyl (GelMA)/acrylate β-cyclodextrin (AcCD) double-network adaptable matrix. This composite hydrogel was fabricated based on gradient patterning driven by a magnet and redox-initiated crosslinking in sequence. The smooth gradient distribution was predicted and optimized before fabrication via computer simulation based on magnetic resonance imaging (MRI) and histological data. Continuous MagHA gradation contributes to the natural generation of mechanical and magnetism gradients to gain a multileveled continuous gradient hydrogel. Subsequently, such gradient hydrogel is implanted into an osteochondral defect. This comprehensive strategy achieves an ideal regeneration for the full-thickness cartilage-to-subchondral bone interface that facilitate cell infiltration and guided depth-dependent cell differentiation.

2. Results and Discussion

2.1. De Novo Design and Synthesis of MagHA

The smooth HA mineral gradient, naturally formed in native full-thickness osteochondral tissue, could gradually transmit mechanical signals from cartilage to bone region, hence enabling a function conversion from lubrication to load-bearing.[6] Therefore, compared with a layer-designed scaffold with a discontinuous gradient, a HA gradient scaffold with smooth increments could better mimic the inherent gradient of osteochondral tissue, which is highly desired for clinical practice.[31–33] In a viscous hydrogel precursors solution, although a HA gradient may be formed through natural gravity settling, the process to obtain a steady gradient is time-consuming and complicated.

Driven by magnetic force, MagHA provides an efficient approach to control the movement of particles. As shown in **Figure 1**A,C and Figure S1C (Supporting Information), the MagHA was synthesized via nucleating HA nanorods on the Fe_3O_4 NPs. Fe and Ca elements were simultaneously detected in both X-ray photoelectron spectroscopy (XPS) and energy dispersive spectroscopy (EDS). The MagHA displays black color and can be attracted by a magnet, indicating its superior paramagnetism (Figure 1B). Notably, MagHA with various amounts of Fe_3O_4 (10 wt%, 20 wt%, and 30 wt%) were prepared and designated as 10% MagHA, 20% MagHA, 30% MagHA for simplification. The scanning electron microscope (SEM) images show that both 10% and 20% MagHA exhibit homogeneous and rod-like shapes; while the 30% MagHA sample displays severe aggregation of Fe_3O_4 NPs and deformed morphology (Figure 1D). Transmission electron microscope (TEM) observation revealed that the Fe_3O_4 NPs in the 20% MagHA sample were evenly distributed and embedded in the nanorods, showing a more homogeneous distribution than the 10% and 30% MagHA samples (Figure 1E). Due to the lack of sufficient Fe_3O_4 NPs that could act as nucleation cores, the appearance of the 10% MagHA sample is similar to that of pure HA (Figure S1, Supporting Information).[34] Only a small portion of nanorods contain Fe_3O_4 NPs. As for the 30% MagHA sample, conversely, many spherical Fe_3O_4 NPs aggregated and were exposed out of nanorods, suggesting the oversupplied nucleation sites for HA growth. Confirmed by the analysis of dynamic light scattering (DLS), the presence of the small-sized particles in the 30% MagHA sample should be ascribed to the aggregation of Fe_3O_4 NPs and the deformed nanorods (Figure 1F). The formed nanorods in both the 10% and 20% MagHA samples were both ≈500 nm.

Since the intensity of the magnetism of MagHA directly determines their movement under a magnetic field, the magnetic properties of these MagHA are important for the fabrication of continuous gradients. As shown in Figure 1G, the saturation magnetization of MagHA is proportional to the amount of Fe_3O_4; the values increase in the order of 10% MagHA (3.59 emu g^{-1}) < 20% MagHA (7.84 emu g^{-1}) < 30% MagHA (11.86 emu g^{-1}), as shown by the hysteresis loops measured via vibrating sample magnetometer (VSM). Taken together, 20% MagHA nanorods were selected for further studies in considering the distribution, nanorod morphology, and magnetic susceptibility χ (2.89×10^{-3}) of Fe_3O_4 NPs.

Accordingly, the crystalline structure of 20% MagHA was identified using X-ray diffraction (XRD). As compared to the patterns of pure HA and Fe_3O_4, the characteristic diffraction peaks assigned for both of them could be observed in the XRD profile of the 20% MagHA sample (Figure 1H). High-resolution TEM (HRTEM) images also showed that the specific crystal lattices for both Fe_3O_4 and HA could be observed in 20% MagHA nanorod, which suggested the Fe_3O_4 core did not affect the purity and crystallization of the HA phase (Figures S1A,B, Supporting Information).

One more thing emphasized here was that the MagHA pattern formed under a magnetic field might be unstable in the hydrogel matrix due to the action of gravity. To tackle this issue, acrylated disodium pamidronate (ADP) was utilized to decorate the surface of 20% MagHA to add reactive double bonds to MagHA (Figure 1C and Figure S2, Supporting Information). Thus, the MagHA particles could be covalently linked to the GelMA network after crosslinking, which helps to stabilize the inorganic particles from settling concern.[34] For simplification, hereafter, the 20% MagHA was shortened as MagHA in text and figures.

2.2. Simulation, Fabrication, and Characterization of Magneto-Pattern Smooth Gradient MagHA

To precisely match the gradient structure of implanted hydrogel with that of native osteochondral tissue, we established a magneto-pattern workflow in COMSOL to simulate the formation of MagHA gradient over magnetic exposure time. According to the real cartilage thickness data obtained from healthy animals, an optimized fabrication process was established. On the one hand, since cartilage thickness differs from species to age,[35] the rabbit osteochondral model was used in this study as a proof of concept. The average thickness of lapine knee trochlear cartilage for Zealand white rabbits (weighing ≈3.5 kg) was determined as 0.507 ± 0.025 mm using both magnetic resonance imaging (MRI) and histological staining (**Figure 2**A,B). On the other hand, the hydrogel designed for filling the full-thickness osteochondral defect in the rabbit was a cylinder of 3.5 mm in diameter and 3 mm in height, referring to reports.[32] Thereafter, to simulate the movement of MagHA in the cylinder hydrogel matrix under magnetic force, a static magnetic field was established by using an N42 Ndfeb permanent magnet (ϕ: 30 mm, height: 10 mm, B_{rmax} = 1.12 T). As illustrated in Figure 2C, the magnetic intensity presents a continuous gradient decrease from 460 mT (bottom, 0 mm) to 400 mT (top, 3.0 mm) in the Z-direction throughout the hydrogel height in COMSOL. However, it remains a uniformity in the horizontal R-direction.

By blending MagHA into the hydrogel precursors solution with the presence of a magnet beneath the solution, the motion of the nanorods was simultaneously influenced by the gravity force of the particles themselves, the driving force from the magnet, and the buoyancy force from the viscous solution (Figure 2D). It was observed that ≈20 min was required for the MagHA nanorods at the solution surface to settle down to the bottom of solution (in 3 mm height). The simulation calculation for this settling process was iteratively solved

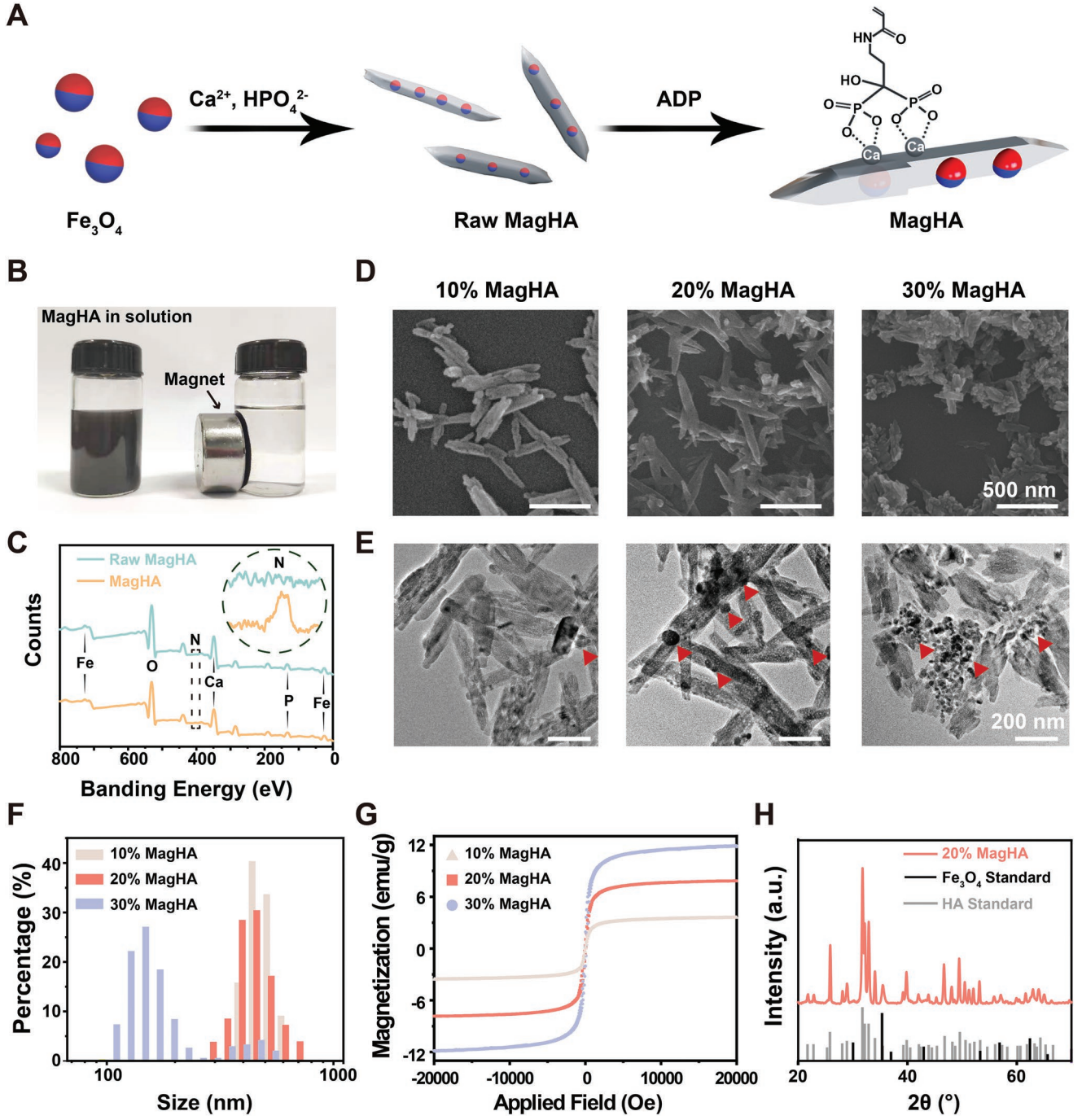

Figure 1. Preparation and characterization of MagHA. A) The schematic fabricating process of MagHA. B) A photo showed the process of MagHA magnetization. C) X-ray photoelectron spectroscopy (XPS) spectrum of raw MagHA and acrylated disodium pamidronate modified MagHA. D,E) The morphology of MagHA nanorods revealed in SEM (D) and TEM (E) images. F) Particle size and size distribution were determined via dynamic light scattering (DLS). G) Hysteresis loops of various MagHA nanorods measured via vibrating sample magnetometer (VSM). H) X-ray diffraction (XRD) results showing the crystalline structure of 20% MagHA, which was compared to the standard patterns of HA (PDF#74-0566) and Fe_3O_4 (PDF#19-0629).

through MATLAB, and the experimental parameters were listed in Table S1 (Supporting Information). However, the rod-like MagHA should be transferred into equivalent spherical nano-objects to conduct the computational calculation according to the equations in supplementary information. In this workflow, MagHA were patterned into transitional gradient distribution over the exposure time to magnetic force (Figure 2E). Only 4 min later, the vast majority of the nano-objects have moved to the middle and lower part of the system, leaving ≈500 µm blank zone at the top, which precisely matches the average thickness of knee trochlea cartilage in the rabbit model (Figure 2A,B). Hence, this simulation result supported the feasibility of

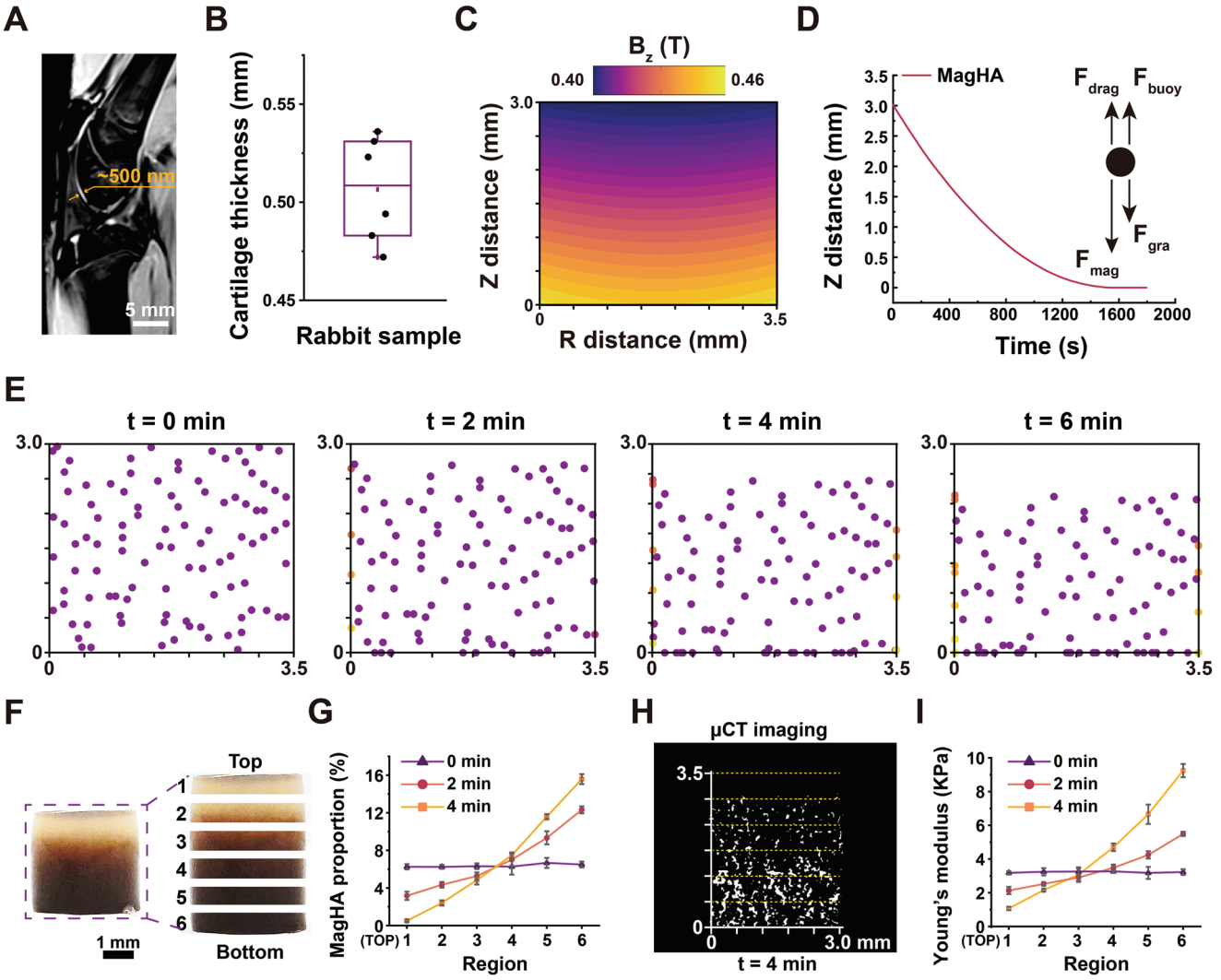

Figure 2. Fabrication and characterization of the hierarchical hydrogel with continuous MagHA gradients. A) MRI image of healthy rabbit knees (sagittal view, yellow arrow pointing highlighted cartilage). B) The cartilage thickness of rabbit samples obtained from MRI images (n = 6). C) COMSOL model of the magnetic field across a diametric cross-section of the hydrogel provided by a N42 permanent magnet. D) MATLAB simulation of a MagHA NP movement in the viscous hydrogel precursor solution. E) Simulation of 100 nano-objects moving over 6 min of magnetic field exposure. F) The gross appearance of the obtained MagHA gradient composite hydrogel under 4 min magnetic field exposure. The obtained hydrogel was sliced into 6 parts with equal thickness for further characterization. G) Thermogravimetric analysis (TGA) analysis showing the mineral proportion. H) Microcomputed tomography (μCT) image of MagHA gradient hydrogel. I) Young's modulus determined for different layers of MagHA gradient hydrogel.

magneto-aligning MagHA motion in a viscous hydrogel precursor solution, and the viscosity of about 8.5 centipoises listed in Table S1 (Supporting Information) for calculation was measured from the pre-hydrogel solution containing 8% GelMA and 8% AcCD.

With the guidance of this prediction, MagHA were mixed into the GelMA/AcCD solution that had been cast into a cylinder mold (diameter: 3.5 mm; height: 3 mm) with the setting of a magnet at the bottom. After standing by for 4 min, a continuous dark gradient pattern could be observed in the Z-direction, leaving a transparent layer on the top. Thereafter, the obtained system was moved to an oven thermoset at 60 °C to complete the crosslinking process, which is redox-initiated by the sodium persulfate (20 mM) and tetramethylethylenediamine (20 mM) in the solution (Figure 2G). It should be noted that a redox initiation system was utilized here to replace the frequently-used UV photo-crosslinking method because black MagHAcould reduce light diffusion.

To further investigate the composition and properties of the continuous MagHA gradient, the composite hydrogel was vertically sectioned into 6 pieces (marked from 1 to 6), which were analyzed individually by thermogravimetric analysis (TGA) and tensile test (Figure 2G,I). If the as-mixed solution was crosslinked (t = 0 min), i.e., no MagHA nanorod having time to move before being fixed, all the 6 layers contain the same amount of MagHA (≈6.3 wt% corresponding to the dry weight of GelMA + AcCD), hence exhibiting similar mechanical modulus. However, for the suspension applied with 2 min magnetic treatment, the even distribution of MagHA had changed into a gradient pattern as the amount of MagHA increased

from ≈3.2 wt% in the top layer (layer 1) to ≈12.3 wt% in the bottom layer (layer 6). Upon magneto-driving for 4 min, the MagHA content in layer 1 was further reduced to ≈0.5 wt%; correspondingly, the MagHA content in layer 6 was raised to ≈15.6 wt% (Figure 2G). This continuous distribution of the mineral component in the final composite hydrogel was further visualized via microcomputed tomography (μCT). As shown in Figure 2H, the μCT image reveals the continuous MagHA gradient in the vertical direction, which is in good agreement with TGA results. Obviously, due to the reinforcement effect of inorganic particles, the 6 layers collected from the composite hydrogel displayed increasing Young's modulus in line with the MagHA content (Figure 2I). Taken together, the obtained composite hydrogel presented a smooth mineral variation, which could closely mimic the contrast from soft hyaline cartilage to hard bone in terms of composition, mechanical properties, as well as, magnetic intensity related to the Fe_3O_4 amount.

2.3. Continuous Gradient Adaptable Hydrogel Promotes Stem Cell Bi-Differentiation

It is known that an ideal implant allow easy infiltration and proliferation of cells, which significantly improve the regenerative outcome. The adaptable hydrogel containing reversible cross-linked sites (including ionic bonds, host-guest interactions, etc.) can be remolded by cellular traction, which supports cell migration within the hydrogel network. In this case, we synthesized GelMA (acrylate grafting degree being ≈20%) and AcCD (having 1.37 acryloyl group per β-cyclodextrin molecule) (Figures S3A,B, Supporting Information). These two components can be integrated through host-guest interactions and partial double-bond crosslinks, forming a DN hydrogel that exhibits higher mechanical strength than the corresponding pure GelMA hydrogel (Figure S3C, Supporting Information).[36,37] By comparing the rheological data of the GelMA and DN hydrogels, under the shear strain of 200%, the hydrogel was destroyed (Figure S3D,E, Supporting Information). The storage modulus (G') of both hydrogels dropped down below their loss modulus (G''), indicating their transformation from a gel state (under 10% strain) to a solution state. Under the cyclic 10% – 200% strain evaluation, the microstructure of the GelMA hydrogel was destroyed under the high strain and was irrevocable due to the lack of self-healing capacity in the network. Differently, the DN hydrogel exhibited clear sol-gel transition alongside the cyclic strain change, benefiting from its reversible host-guest interaction.

Stress relaxation is a key characteristic of capability of hydrogel supporting cell-ECM interactions in initial fracture haematomas.[14] The host-guest crosslinking sites in DN hydrogel can be destroyed by a small force from cell traction and allow the clustering of the integrin receptors binding to the ligating domains in gelatin, thereby leading to extensive cell-matrix interactions and adapting cell spreading and migration (Figure S4, Supporting Information). Hence, we next investigated the stress variation of GelMA and DN hydrogel under a constant strain of 15%. As depicted in **Figure 3**A, the DN hydrogel can relax over 50% stress within 1000 s, which is unachievable for the GelMA hydrogel. This result suggested that mechanical remodeling of DN hydrogel can be driven by the cells. Hence, bone marrow mesenchymal stromal cells (BMSCs) seeded on the hydrogels could migrate into the inner part of the DN hydrogel after 7 days of culture; however, for GelMA hydrogel, the majority of the seeded cells are mainly distributed on the surface ofhydrogel (Figure 3B).

We next sought to examine the in vitro performance of GelMA/AcCD DN hydrogel matrix. Ideally, stem cells migrate and obtain guiding signals from surrounding tissue, and differentiate into a series of cell lineages leading to the replacement of damaged ECM and eventually tissue remodeling. The afore-fabricated composite hydrogel consisting of the MagHA gradient and the DN hydrogel was expected to meet these requirements (Figure 3C). To facilitate differentiation study in vitro, several hydrogels were prepared, including the pure DN hydrogel, the HACH hydrogel (i.e., blending conventional HA nanorods with the DN hydrogel to form composite hydrogel), and the MagCH hydrogel (i.e., blending MagHA nanorods with the DN hydrogel to form composite hydrogel).

Having confirmed the excellent biocompatibility of various hydrogels (Figure S5, Supporting Information), we continued to evaluate their capacity in inducing the chondrogenic or osteogenic differentiation. The MagCH(-) and MagCH(+) represent the culture being conducted in the absence or presence of magnetic field (50 mT).[38] First, we applied immunofluorescent staining on Sox9 (chondrogenic) and osteocalcin (OCN, osteogenic) expressions for BMSCs after 14 days of incubation on hydrogels under different situations, using the cells on tissue culture polystyrene (TCPs) as blank control. As shown in Figure 3D,E, the highest Sox9 expression was found on the DN hydrogel; then its level was ranked in a descending order as follows: HACH ≈ MagCH(-) > MagCH(+). Conversely, the highest OCN expression was detected on the MagCH(+) hydrogel, followed by MagCH(-) ≈ HACH and DN groups. Subsequently, we quantitatively measured the expressions of collagen II (Col-II) and glycosaminoglycan (GAG) in chondroinductive medium, as well as the expressions of collagen I (Col-I) and alkaline phosphatase (ALP) in osteoinductive medium. Obviously, the increasing/declining trend for these chondrogenic and osteogenic markers was in accordance with the above immunofluorescent staining outcomes (Figure 3F,G). Collectively, the DN hydrogel favored chondrogenic differentiation, while the MagCH hydrogel facilitated osteogenic differentiation, specifically, with magnetic stimulus being supplied. The DN hydrogel free of inorganic components is soft, with gelatin as its major component to match the needs for chondrogenesis. The HA containing HACH and MagCH hydrogels are stiffer than the DN hydrogel, together with the capacity to provide calcium and phosphate cues, consequently promoting osteogenesis.[39–41] Of note, although the MagCH(-) and HACH shared similar results in these assays, the MagCH(+) hydrogel achieved the most efficient osteoinductivity outcome. In the osteochondral defects, the MagHA-gradient DN hydrogel would promisingly allow BMSCs to flood from the bone cavity and grow into the matrix. These BMSCs were liable to be smoothly polarized into chondrocyte-osteocyte two directions under the tissue-specific guidance mimicking the osteochondral interface.

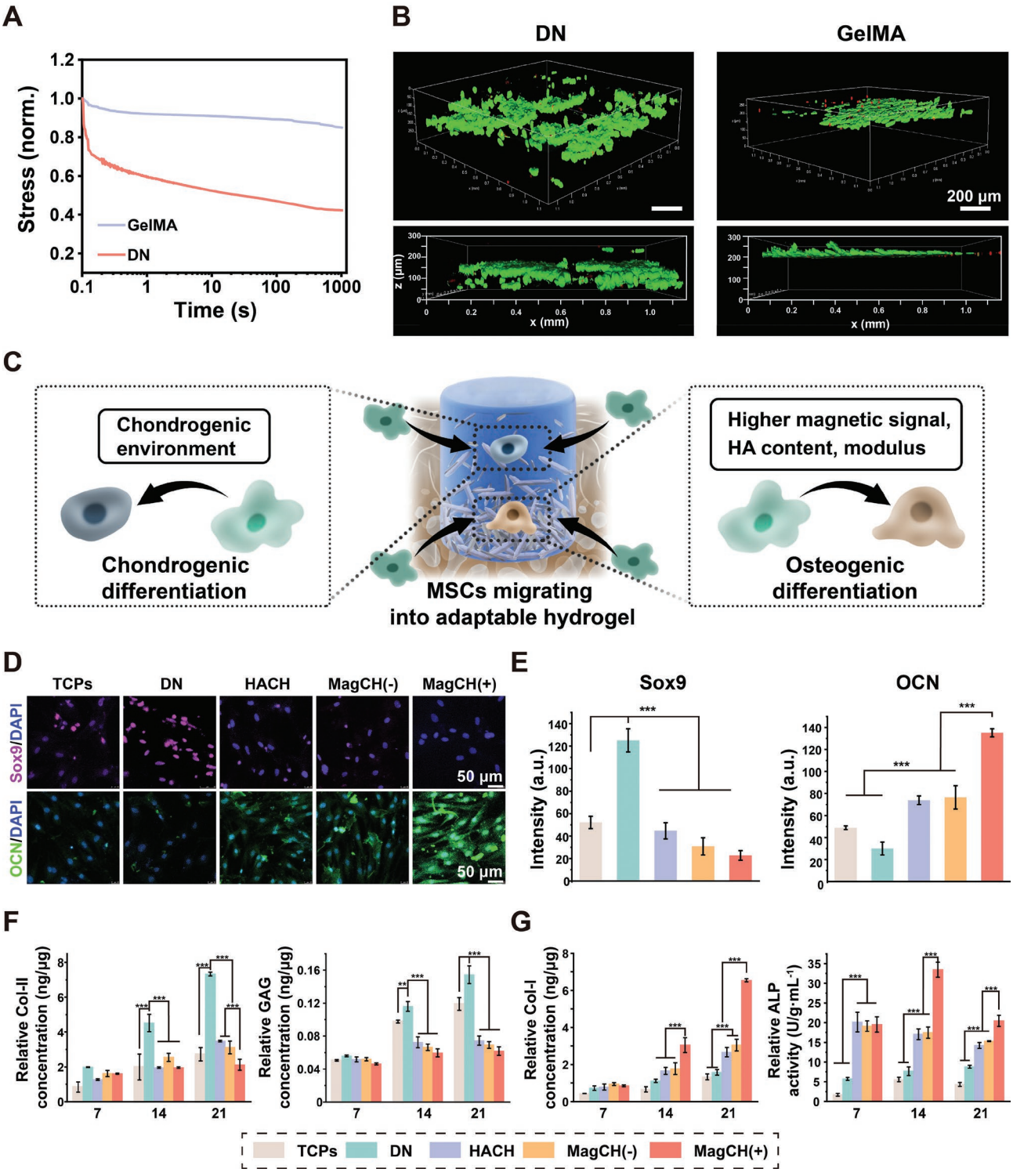

Figure 3. Fabrication of the GelMA/AcCD double-network (DN) hydrogel matrix and evaluations of cell behaviors in different hydrogels. A) Stress relaxation of the DN hydrogel. B) Confocal laser scanning microscopy (CLSM) showing the migration of bone marrow mesenchymal stromal cells (BMSCs) in the adaptable DN hydrogel. C) Schematic illustration showing the adaptable hydrogel directs chondrogenic and osteogenic differentiation. D) CLSM images and E) the corresponding fluorescent intensity quantified via ImageJ showing the expression of chondrogenic (Sox9) and osteogenic (osteocalcin, OCN) protein for BMSCs cultured in groups of TCPs (i.e., the cells on tissue culture polystyrene) control, HA nanorods + DN composite hydrogel (HACH), MagHA nanorods + DN composite hydrogel without (MagCH(-)) and with the application of magnetic field (MagCH(+)) for 14 days. F) The quantitative chondrogenic expressions including collagen II (Col-II) and glycosaminoglycan (GAG) for BMSCs at day 7, 14, and 21 after various treatments. G) The quantitative osteogenic expressions including collagen I (Col-I) and alkaline phosphatase (ALP) for BMSCs at day 7, 14, and 21 after various treatments. *P < 0.05, **P < 0.01, and ***P < 0.001, n = 6.

2.4. In Vivo Implantation for Full-Thickness Osteochondral Regeneration

To acquire a deeper understanding of the regenerative outcome of the MagCH hydrogel, in vivo study was carried out. Cylindrical defects (diameter: 3.5 mm; depth: 3 mm) were drilled at the trochlear sites using the rabbit knee joint model, and the rabbits were randomly divided into five groups for the evaluation of osteochondral regeneration: Control (treated with saline solution), Blank (filled with the DN hydrogel), BiH (filled with a bi-phasic hydrogel with an upper DN hydrogel layer of 500 μm in thickness settled on MagCH layer of 2.5 mm in thickness), Gra- (filled with MagHA gradient hydrogel without magnetic stimuli), and Gra+ (filled with MagHA gradient hydrogel with external magnet device application).

The magnet device used in this study was established with two thin titanium-encapsulating (to avoid erosion in vivo) magnet pieces buried symmetrically at the two sides of the joint inside subcutaneous fascia layers (sutured onto tissue to fix them for avoiding displacement), providing a moderate static magnetic field of about 50 mT (**Figure 4**A).[42] Six and twelve week post-operation, the animals were euthanized, and the joints were explanted and subjected to standardized macroscopic, MRI image, histological, μCT, and immune-histochemical staining characterizations to monitor the osteochondral regeneration process. All analyses of 12-week post-operation are provided in Figures 4 and 5, and those 6-week data are put in the supplementary information (Figure S6, Supporting Information).

At 12 weeks post-surgery, the defects in the Control and Blank groups were still not filled, being accompanied by joint effusion. As for the BiH group, it was renewal fibrosis tissue covering the injury while displaying discontinuity through gross observation (Figure 4B); by comparison, both the Gra- and Gra+ groups successfully achieved obvious regeneration of analogous hyaline cartilage. Of note, the newly formed hyaline cartilage was more mature in the Gra+ group without a distinguished fissure. Surprisingly, in the Gra+ group, the regenerated tissue was completely integrated with surrounding tissue, which is similar to native hyaline cartilage. Further, we applied the international cartilage repair society scoring system (ICRS) to semiquantitatively evaluate these macroscopic results based on Table S2 (Supporting Information).[43] The results were ranked as: Gra+ > Gra- > BiH > Blank > Control, showing significant differences between groups (Figure 4F). The discrepancy between the Gra-(+) and BiH groups reached a highly significant p value of 0.007. Promisingly, the Gra+ showed the best gross appearance, whose p value versus the BiH group was further reduced to < 0.001, also, showing a significant difference to the Gra- group ($p = 0.025$).

MRI was then employed to visualize the formation of new cartilage and the sub-cartilage areas. As shown in Figure 4C, the defects located where red arrows pointed (the centre of the trochlea part). These scan results were in good agreement with the gross evaluations. Unfilled defects remained in both the Control and Blank groups at 12-weeks post-operation, while incomplete and coarse cartilage with obvious cracks was regenerated in the BiH group, displaying no closure of the bone plate. The Gra- group exhibited relatively integrated morphology associated with tissue regeneration, but remained a clear margin between the neo-cartilage and bone plate, as well as, the cartilage surface being rugged. However, the Gra+ group eliminated this insufficiency in osteochondral repairing, revealing smooth and even cartilage integrating well with the surrounding native cartilage. Overall, all the above macroscopic morphology outcomes collectively demonstrated that the combination of the smooth MagHA gradient and the external magnetic stimulus could effectively induce analogous osteochondral tissue regeneration in an accelerated mode. It was proposed that the Gra+ group not only has taken advantage of the biochemical and biophysical cues provided by the MagHA gradient, but also utilized the electromagnetic physiological nature of native bone tissue to promote osteochondral regeneration under the persistent magnetic stimulus.[40–42]

Next, the joint samples were sliced and assessed with their histomorphometric outcomes. We stained tissue slices with hematoxylin & eosin (H&E) and toluidine blue. Based on the colored images (Figure 4D,E), we evaluated them with Wakitani's[44] and Seller's[45] histological scoring systems (Tables S3 and S4, Supporting Information), which roundly analyzed the full-thickness osteochondral tissue from cartilage to bone, and from cellular morphology to adjacent integration (Figure 4G and 4H).[46] Accordingly, both the Gra- and Gra+ groups distinguished themselves from other groups in these evaluations. The highest Wakitani's score and the lowest Seller's score were obtained for the Gra+ group, followed by the Gra- group, presenting remarkably improved efficiency in regenerating the injured cartilage-to-bone interfacial tissue. The Wakitani's score presented significant difference between random two groups: Gra+ ($p = 0.004$ vs Gra-; $p < 0.001$ vs BiH), Gra- ($p = 0.007$ vs BiH; $p < 0.001$ vs Blank), and BiH ($p = 0.016$ vs Blank; $p < 0.001$ vs Control), so as to Seller's score. From Figure 4D,E, the growing tissue in the Gra+ group exhibited hyaline-like cartilage, radial chondrocyte columns in the deep zone of cartilage, aligned tidemark, closure bone plate, as well as a considerable degree of GAG production. Comparatively, the Gra- group showed a slightly inferior result, such as less GAG secretion and less perfect micromorphology. As for the BiH group, fiber texture was dominant in the renewal cartilage, and few neo-bone has grown to the horizontal line of the trochlear bone plate. The Blank and the Control group presented the worst outcome, even with some granulation tissue still being detectable. These two groups did not provide any extra signal to induce bone end generation, which also delayed cartilage restoration.

The formation of new subchondral bone was evaluated with reconstructed μCT images qualitatively (Figure 4I) and quantitatively (Figure 4K,L).[47] As shown in the pictures, in the Gra+ group, newly formed bone tissue had filled the defect area densely with the successful closure of the bone plate, while there was still an obvious hole in the center of Gra- implanted defect. In the other three groups, less and thinner sclerotin was shown in the images. It should be noted that relatively abundant minerals had deposited in the bottom half of BiH implant, i.e., at the site where MagCH hydrogel located, while not for the upper DN hydrogel, which revealed the possible lamination effect causing adverse influence in interfacial tissue regeneration.[25] Specifically, the bone volume proportion (BV/TV) in the

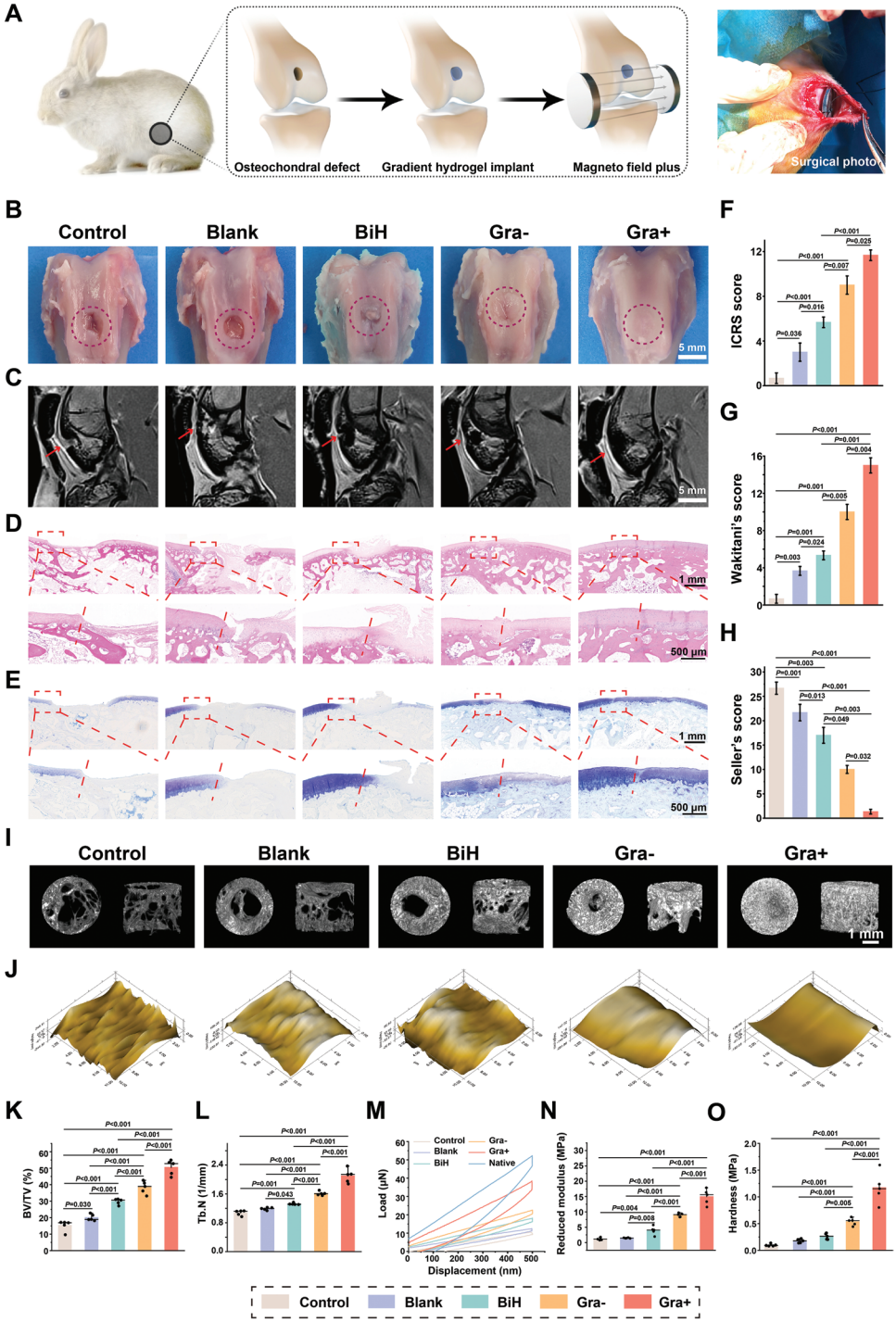

Figure 4. In vivo repair (12 weeks post surgery) of osteochondral defects by different approaches in rabbit knee joint model. A) A schematic of surgery processes for rabbit knee joint model. B) The gross images of the repaired osteochondral defects in groups of Control (treated with saline solution), Blank (filled with the DN hydrogel), BiH (filled with a bi-phasic hydrogel with an upper DN hydrogel layer of 500 μm in thickness settled on MagCH layer of 2.5 mm in thickness), Gra- (filled with MagHA gradient hydrogel without magnetic stimuli), and Gra+ (filled with MagHA gradient hydrogel with external magnet device application)) (defects inside the dotted circles). C) MRI images of the repaired osteochondral defects in each group (arrows pointing to the defects). D,E) Histological images of hematoxylin & eosin (H&E) (D) and toluidine blue staining (E). F) The international cartilage repair society scoring system (ICRS) macroscopic scores for gross observations. G,H) Wakitani's scores G) and Seller's scores H) for histological evaluation. I) Reconstructed 3D μCT images of the repaired subchondral bone tissues in each group. J,K) The volume ratio of the newly formed bone to the total volume of defect region (BV/TV) and corresponding trabecula number (Tb.N) analyzed from μCT images. L) The surface geomorphology of the repaired tissues acquired by nanoindentation tests. M) Representative load-displacement loops determined for repaired tissues in each group. N,O) The biomechanical properties of repaired tissue investigated by reduced modulus (N) and hardness (O). *P < 0.05, **P < 0.01, and ***P < 0.001, n = 6.

Gra+ group reached 50.51 ± 4.09% with the highest trabecular number (Th.N), which is greatly higher than those of the other groups ($p < 0.001$ versus Gra-, BiH, Blank, and Control). The important contribution of the smooth MagHA gradient to subchondral bone regeneration could be identified via contrasting the Gra- and BiH group ($p < 0.001$), while the synergistic promotion effect of the applied external magnetic field was confirmed by comparing the Gra+ and Gra- group ($p < 0.001$). In accordance with the aforementioned neo-cartilage formation, these results of neo-subchondral bone formation highlighted the tight connection and mutual influence between the two distinguishable parts in interfacial tissue repairing. This inspired that the cartilage maturation and performance can hardly be guaranteed unless the subchondral bone can provide good support.

To further verify this statement, we implemented a nanoindentation test to investigate the biomechanical properties of a regenerated articular surface, which would add evidence to prove if the newborn cartilage could remain stable in the complex environment of the joint. As displayed in Figure 4J, the surface of the cartilage repaired in the Gra- or Gra+ group was smooth; while the surfaces were rather rough and scraggy for Control, Blank, and BiH groups. Load-displacement curves were obtained for all repaired cartilage samples, together with the pattern of native cartilage for comparison (Figure 4M). Undoubtedly, the Gra+ group presented a loop closely resembling that of the native one, followed by Gra- and the next BiH group. The reduced moduli measured for the regenerated osteochondral tissue in the Gra+ was 16.61 ± 0.95 MPa, which was 13.5, 11.53, 4.22, and 1.82 times higher than those of the Control, Blank, BiH, and Gra- groups, respectively. Notably, this value was close to the average native reduced modulus (22.58 ± 3.26 MPa) (Figure 4N).[30] Consistently, the hardness of newborn tissues declined in the same order with the Gra+ group showing the highest value (Figure 4O). To sum up, Gra+ strategy exhibited a promising performance in full-thickness osteochondral regeneration, whose multileveled gradations in mineral, mechanical strength, and magnetism facilitate the defect restoration and upregulating performance reconstruction.

2.5. Investigation on the Hierarchical and Anisotropic Feature of Reconstructed Osteochondral ECM

Interfacial osteochondral tissue is built upon a gradually variational ECM matrix, especially in terms of collagen constituent transition and anisotropic collagen orientation from the cartilage zone to the bone zone. This character guarantees the basic functions of joints and protects skeletal bone from destruction. Hence, the ultimate goal of osteochondral regeneration is to regain these tissue-specific features. Therein, immunohistochemistry staining was employed to visualize the expression and distribution of Col-II, collagen type X (Col-X), and Col-I. Referring to the standard native sample (positive control), Col-II would only locate precisely in the cartilage area as a typical symbol of hyaline cartilage, and Col-I was mainly distributed in the bone area beneath the tidemark line, with the expressions of Col-X indicating the formation of calcified cartilage interlayer between the two areas. Based on this, the brown color indicating the immunohistological staining on Col-II, Col-X, and Col-I could be observed in different intensities for the regenerated osteochondral tissues with different treatments (**Figure 5**A). The highest Col-II staining intensity could be observed in the Gra+ group, followed by the Gra- group. Conversely, only limited Col-II expression could be found in the BiH, Blank, and Control groups, which is in accordance with the aforementioned results on cartilage regeneration. Similarly, the Gra+ group showed high expression of Col-I in the subchondral area, with the Gra- taking second place and the BiH the third, which was consistent with the formation and maturation of neobone tissue. The difference here was that considerable Col-I also existed in the defect areas of the Blank and Control groups. At the same time, it revealed the occurrence of fibrous connective tissue in accord with the H&E and toluidine blue histological staining evaluations. The calcified cartilage interlayer is an important transition zone to connect the cartilage and subchondral bone tissues while isolating two parts and preventing vascularization in cartilage. The expression of rich Col-X suggests the good formation of the calcified cartilage, constructing the tidemark at the transition area. Distinguishedly, among all the cases, the Gra+ and Gra- groups displayed an obviously-positive Col-X staining. In contrast, the osteochondral interface in the Gra+ group was integrated with the upper and lower zones the most tightly.

Furthermore, the collagen fiber orientation was shown in sirius red staining and polarizing light microscope observation (Figure 5B and Figure S8, Supporting Information). In native articular cartilage, the collagen fibers in the surface zone are horizontal, while those in the middle and deep cartilage zone are vertical to the surface. This heterogeneous and anisotropic pattern plays a significant role in stress dispersion and transition toward subchondral bone. For all the repaired samples, the predominant angle of collagen fiber orientation was calculated by the Directionality plugin in ImageJ software. According to the native cartilage structure, two separate regions of interest (ROI) were selected for analysis, i.e., the upper 1/3 zone under cartilage surface (Surface zone), and the middle-to-deep zones at the bottom 2/3 of cartilage (Base zone). Results of collagen fiber orientations in these two zones are provided in Figure 5C,D. In the Control and Blank groups, most collagen fibers oriented horizontally (i.e., 0°) in both the Surface and Base zone, indicating that only fibrous connective tissue existed and covered the defect area. For the BiH group, ≈50% of the collagen fibers in the Surface zone were aligned between -20° and 20°, with only ≈25% of collagen fibers located in the vertical direction of (±) 60°-90°, also revealing a random fibrous tissue in major. The regenerative effect took a turn for the better in the Gra- and Gra+ groups. For the Gra- group, the parallel collagen fibers in the surface zone were up to approx. 78%, and the collagen alignment distributed in the direction of (±) 60°-90° was also increased to ≈40%. Compared to the data of native tissue (Surface zone: ≈90% in the horizon, Base zone: ≈75% in the vertical direction), the Gra+ group reached the data of ≈88% parallel collagen fibers in Surface and ≈52% vertical collagen fibers in Base zone, which were the closest result toward the native sample.

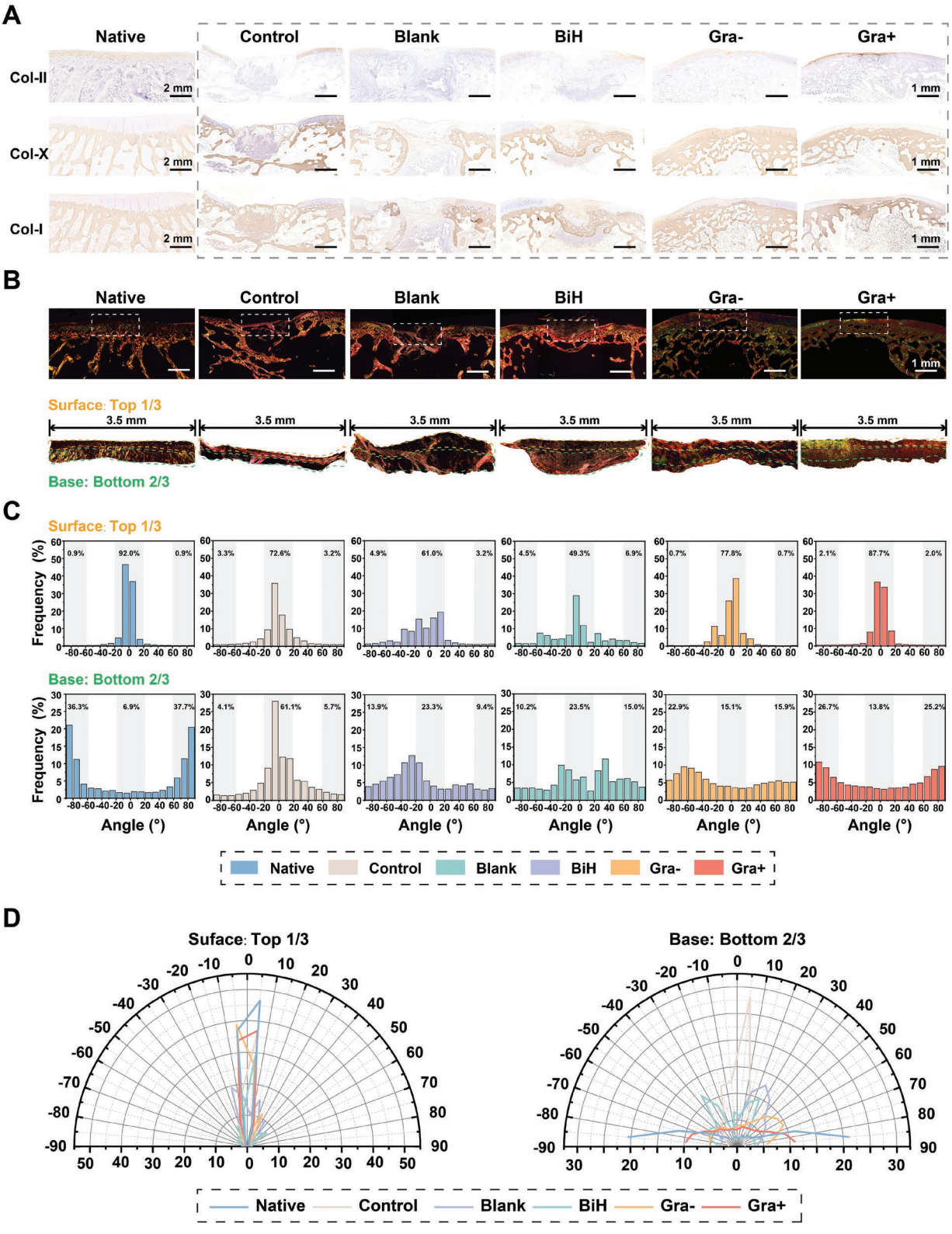

Figure 5. Hierarchical collagen expression and quantitative analyses of collagen fiber distribution of the repaired tissues with different treatments at 12 weeks post-surgery. A) Immunohistological staining for Col-II, collagen type X (Col-X), and Col-I to indicate the smooth multi-gradient composite hydrogel showing a synergistic promotion effect on the regeneration of cartilage and subchondral bone tissues. B) Sirius red staining on collagen fibers in regenerated tissues and normal healthy cartilage. A polarizing light microscope was utilized for the quantitative analysis of collagen fiber orientation in the Surface zone (upper 1/3) and Base zone (bottom 2/3) (n = 6). C,D) Comprehensive comparison of collagen fiber orientation within Surface and Base areas using native tissue as reference (C) and further presented by polar coordinates (D).

3. Conclusion

In conclusion, we have developed a composite hydrogel with multileveled smooth gradients for the regeneration of full-thickness osteochondral tissue. To obtain a HA gradation that can mimic the stepwise increasing mineral content in cartilage-to-subchondral bone transition, magnetic force was proposed to control the movement of MagHA to form a continuous gradient pattern. Importantly, the homogeneous morphology and sufficient magnetization of MagHA enable rapid fabrication of a continuous MagHA gradient. To better mimic the clinical practice, the cartilage thickness in a real rabbit knee joint was measured based on diagnostic MRI images, and a finite element simulation platform was applied to simulate the mobility of MagHA in hydrogel precursors solution over the exposure time of magnetic field. These results provided essential guidance for the preparation of smooth MagHA gradient hydrogel implants for the precise reconstruction of the respective osteochondral tissue. Promisingly, this MagHA gradient could generate additional gradations in mechanical properties and magnetism intensity in line with MagHA amount.

Associated with an external magnetic stimulus, it was evidenced that this Gra+ construct provided tissue-specific cues for cell differentiation and heterogeneous interfacial tissue regeneration. Notably, the adaptable DN hydrogel composed of GelMA and AcCD played essential roles in facilitating cell infiltration, proliferation, and spreading. Overall, this is the first study combining magneto-driven smooth MagHA gradient with persistent magnetic stimulus to emulate native osteochondral ECM. A generalized adoption of this strategy may lead to the development of novel therapeutics for osteochondral regeneration. We envision that the multilevel hierarchical hydrogel will serve as a valuable platform for regenerative medicine.

Supporting Information

Supporting Information is available from the Wiley Online Library or from the author.

Acknowledgements

The authors acknowledged the financial support from National Key R&D Program of China (2018YFE0194400), National Natural Science Foundation of China (U22A20159), Fundamental Research Funds for the Central Universities (buctrc202220), Beijing Natural Science Foundation (72321000), and the SINOPEC project (421029). The authors thank Shen Ye for the formula derivation of the volume calculation of MagHA nanorods. The animal experiment protocol was approved by the Animal Care and Use Committee of Peking University Third Hospital (jmy2020-09-01).

Conflict of Interest

The authors declare no conflict of interest.

Data Availability Statement

The data that support the findings of this study are available from the corresponding author upon reasonable request.

Keywords

biochemical gradient, biophysical gradient, continuous gradient, magnetic stimulus, osteochondral regeneration

Received: October 17, 2022
Revised: January 31, 2023
Published online: March 30, 2023

[1] A. Guermazi, D. Hayashi, F. W. Roemer, J. Niu, E. K. Quinn, M. D. Crema, M. C. Nevitt, J. Torner, C. E. Lewis, D. T. Felson, *Arthritis Rheumatol* **2017**, *69*, 560.
[2] J. M. Bert, *Arthroscopy* **2015**, *31*, 501.
[3] H. Kwon, W. E. Brown, C. A. Lee, D. Wang, N. Paschos, J. C. Hu, K. A. Athanasiou, *Nat. Rev. Rheumatol.* **2019**, *15*, 550.
[4] X. Niu, N. LI, Z. Du, X. Li, *Bioact Mater* **2023**, *20*, 574.
[5] C. Li, L. Ouyang, J. P. K. Armstrong, M. M. Stevens, *Trends Biotechnol.* **2020**, *39*, 150.
[6] L. Zhou, V. O. GJVM, J. Malda, M. J. Stoddart, Y. Lai, R. G. Richards, K. Ki-wai Ho, L. Qin, *Adv. Healthcare Mater.* **2020**, *9*, 2001008.
[7] S. Ansari, S. Khorshidi, A. Karkhaneh, *Acta Biomater.* **2019**, *87*, 41.
[8] A. K. Gaharwar, I. Singh, A. Khademhosseini, *Nat. Rev. Mater.* **2020**, *5*, 686.
[9] Y. Chen, M. Ma, H. Cao, Y. Wang, Y. Xu, Y. Teng, Y. Sun, J. Liang, Y. Fan, X. Zhang, *J. Mater. Chem. B* **2019**, *7*, 3993.
[10] I. Calejo, R. Costa-Almeida, R. L. Reis, M. E. Gomes, *Trends Biotechnol.* **2020**, *38*, 83.
[11] L. Zhang, L. Fu, X. Zhang, L. Chen, Q. Cai, X. Yang, *Biomater. Sci.* **2021**, *9*, 1547.
[12] J. Yang, Y. Li, Y. Liu, D. Li, L. Zhang, Q. Wang, Y. Xiao, X. Zhang, *Acta Biomater.* **2019**, *91*, 159.
[13] L. Zheng, S. Liu, X. Cheng, Z. Qin, Z. Lu, K. Zhang, J. Zhao, *Adv. Sci.* **2019**, *6*, 1900099.
[14] O. Chaudhuri, L. Gu, D. Klumpers, M. Darnell, S. A. Bencherif, J. C. Weaver, N. Huebsch, H. p. Lee, E. Lippens, G. N. Duda, D. J. Mooney, *Nat. Mater.* **2016**, *15*, 326.
[15] C. Loebel, R. L. Mauck, J. A. Burdick, *Nat. Mater.* **2019**, *18*, 883.
[16] a) J. A. Burdick, W. L. Murphy, *Nat. Commun.* **2012**, *3*, 1269; b) H. Wang, S. C. Heilshorn, *Adv. Mater.* **2015**, *27*, 3717.
[17] a) M. W. Tibbitt, K. S. Anseth, *Sci. Transl. Med.* **2012**, *4*, 160ps24; b) K. Zhang, Q. Feng, Z. Fang, L. Gu, L. Bian, *Chem. Rev.* **2021**, *121*, 11149.
[18] A. M. Rosales, K. S. Anseth, *Nat. Rev. Mater.* **2016**, *1*, 15012.
[19] a) J. Park, S. Murayama, M. Osaki, H. Yamaguchi, A. Harada, G. Matsuba, Y. Takashima, *Adv. Mater.* **2020**, *32*, 2002008; b) K. Miyamae, M. Nakahata, Y. Takashima, A. Harada, *Angew. Chem., Int. Ed.* **2015**, *54*, 8984.
[20] L. Sardeli, D. P. Pacheco, L. Zorzetto, C. Rinoldi, W. Swieszkowski, P. Petrini, *J. Appl. Biomater. Func.* **2020**, *226*, 119536.
[21] J. Dou, S. Mao, H. Li, J.-M. Lin, *Anal. Chem.* **2020**, *92*, 892.
[22] M. E. Prendergast, J. A. Burdick, *Adv. Mater.* **2020**, *32*, 1902516.
[23] C. Li, L. Ouyang, I. J. Pence, A. C. Moore, Y. Lin, C. W. Winter, J. P. K. Armstrong, M. M. Stevens, *Adv. Mater.* **2019**, *31*, 1900291.
[24] J. P. K. Armstrong, J. L. Puetzer, A. Serio, A. G. Guex, M. Kapnisi, A. Breant, Y. Zong, V. Assal, S. C. Skaalure, O. King, T. Murty, C. Meinert, A. C. Franklin, P. G. Bassindale, M. K. Nichols, C. M. Terracciano, D. W. Hutmacher, B. W. Drinkwater, T. J. Klein, A. W. Perriman, M. M. Stevens, *Adv. Mater.* **2018**, *30*, 1802649.
[25] C. Li, J. P. K. Armstrong, I. J. Pence, W. Kit-Anan, J. L. Puetzer, S. Correia Carreira, A. C. Moore, M. M. Stevens, *Biomaterials* **2018**, *176*, 24.
[26] G. Xu, Z. Ding, Q. Lu, X. Zhang, X. Zhou, L. Xiao, G. Lu, D. L. Kaplan, *Protein Cell* **2020**, *11*, 267.

[27] C. Zhu, J. Qiu, S. Pongkitwitoon, S. Thomopoulos, Y. Xia, *Adv. Mater.* **2018**, *30*, 1706706.
[28] S. P. Grogan, C. Pauli, P. Chen, J. Du, C. B. Chung, S. D. Kong, C. W. Colwell, M. K. Lotz, S. Jin, D. D. D'Lima, *Tissue Eng., Part C* **2012**, *18*, 496.
[29] Y. Zhang, J. Li, P. Habibovic, *Bioact. Mater.* **2022**, *15*, 372.
[30] S. P. Gorgan, C. Pauli, P. Chen, J. Du, C. B. Chung, S. Kong, C. W. Colwell, M. K. Lota, S. Jin, D. D. D'Lima, *Tissue Eng., Part C* **2012**, *18*, 496.
[31] L. Zhang, L. Fu, X. Zhang, L. Chen, Q. Cai, X. Yang, *Biomater. Sci.* **2021**, *9*, 1547.
[32] W. Dai, L. Zhang, Y. Yu, W. Yan, F. Zhao, Y. Fan, C. Cao, Q. Cai, X. Hu, Y. Ao, *Adv. Funct. Mater.* **2022**, *32*, 2200710.
[33] J. E. Phillips, K. L. Burns, J. M. Le Doux, R. E. Guldberg, A. J. Garcia, *Proc. Natl. Acad. Sci. U. S. A.* **2008**, *105*, 12170.
[34] L. Gu, Y. Zhang, L. Zhang, Y. Huang, D. Zuo, Q, C. , X. Yang, *Biomed. Mater.* **2020**, *15*, 035012.
[35] H. L. Fermor, S. W. D. McLure, S. D. Taylor, S. L. Russell, S. Williams, J. Fisher, E. Ingham, *Bio-Med. Mater. Eng.* **2015**, *25*, 381.
[36] J. Xu, Q. Feng, S. Lin, W. Yuan, R. Li, J. Li, K. Wei, X. Chen, K. Zhang, Y. Yang, T. Wu, B. Wang, M. Zhu, R. Guo, G. Li, L. Bian, *Biomaterials* **2019**, *210*, 51.
[37] Q. Feng, K. Wei, S. Lin, Z. Xu, Y. Sun, P. Shi, G. Li, L. Bian, *Biomaterials* **2016**, *101*, 217.
[38] E.-C. Kim, R. Leesungbok, S.-W. Lee, H.-W. Lee, S. H. Park, S.-J. Mah, S.-J. Ahn, *Bioelectromagnetics* **2015**, *36*, 267.
[39] X. Yang, J. Sun, Z. Liang, F. Zhang, X. J. Liang, G. Yu, M. D. Weir, M. A. Reynolds, G. Ning, H. H. K. Xu, *Biomaterials* **2012**, *183*, 151.
[40] A. Russo, M. Bianchi, M. Sartori, M. Boi, G. Giavaresi, D. M. Salter, M. Jelic, M. C. Maltarello, A. Ortolani, S. Sprio, M. Fini, A. Tampieri, M. Marcacci, *J. Biomed. Mater. Res.* **2018**, *106B*, 546.
[41] A. Gloria, T. Russo, U. D'Amora, S. Zeppetelli, T. D'Alessandro, M. Sandri, M. Banobre-Lopez, Y. Pineiro-Redondo, M. Uhlarz, A. Tampieri, J. Rivas, T. Herrmannsdorfer, V. A. Dediu, L. Ambrosio, R. De Santis, *J. R. Soc. Interface* **2012**, *10*, 20120833.
[42] V. Iacovacci, I. Naselli, A. R. Salgarella, F. Clemente, L. Ricotti, C. Cipriani, *RSC Adv.* **2021**, *11*, 6766.
[43] H. Yin, Y. Wang, X. Sun, G. Cui, Z. Sun, P. Chen, Y. Xu, X. Yuan, H. Meng, W. Xu, A. Wang, Q. Guo, S. Lu, J. Peng, *Acta Biomater.* **2018**, *77*, 127.
[44] L. Goebel, P. Orth, M. Cucchiarini, D. Pape, H. Madry, *Osteoarthritis Cartilage* **2017**, *25*, 581.
[45] R. S. Sellers, D. Peluso, E. A. Morris, *J. Bone Jt. Surg.* **1997**, *97*, 1452.
[46] P. Orth, D. Zurakowski, D. Wincheringer, H. Madry, *Tissue Eng. – Part C ME* **2012**, *18*, 329.
[47] Z. Wan, Z. Yuan, Y. Li, Y. Zhang, Y. Wang, Y. Yu, J. Mao, Q. Cai, X. Yang, *Adv. Funct. Mater.* **2022**, *32*, 2113280.